Thermal Energy Harvesting Plasmonic Based Chemical Sensors

Nicholas Karker, Gnanaprakash Dharmalingam, and Michael A. Carpenter*

SUNY College of Nanoscale Science and Engineering, 257 Fuller Road, Albany, New York 12203, United States

ABSTRACT Detection of gases such as H_2, CO, and NO_2 at 500 °C or greater requires materials with thermal stability and reliability. One of the major barriers toward integration of plasmonic-based chemical sensors is the requirement of multiple components such as light sources and spectrometers. In this work, plasmonic sensing results are presented where thermal energy is harvested using lithographically patterned Au nanorods, replacing the need for an external incident light source. Gas sensing results using the harvested thermal energy are in good agreement with sensing experiments, which used an external incident light source. Principal Component Analysis (PCA) was used to reduce the wavelength parameter space from 665 variables down to 4 variables with similar levels of demonstrated selectivity. The combination of a plasmonic-based energy harvesting sensing paradigm with PCA analysis offers a novel path toward simplification and integration of plasmonic-based sensing methods.

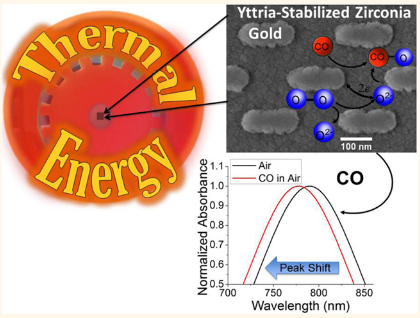

KEYWORDS: thermal harvesting · plasmonic · sensor · harsh environment · PCA

There is a current need for high temperature emission gas sensors for combustion environments such as turbine engines and coal-fired power plants. Reliable and sensitive harsh environment chemical sensors are needed in order to meet the requirements of increasing gas emission regulations within combustion related applications. Any solution to satisfy the current demand of harsh environment sensors would need to be cost-effective and be able to withstand high temperatures (500−800 °C) as well as oxidizing or reducing environments. Development of a variety of metal oxide nanocomposite-based chemical sensing materials and sensing paradigms have shown promise in satisfying these requirements.[1] However, implementation of miniaturized gas sensing technologies in these extreme combustion environments is limited by cost,[2] reliability,[3] and integration barriers.[4] Thermal energy harvesting techniques coupled with plasmonics-based chemical sensing methods and PCA analysis, as demonstrated for the first time in this study, serve as promising and novel sensing paradigms that will satisfy these challenging requirements as well as having broader applications in sensing and catalysis research initiatives.

Plasmonics-based chemical sensing has been shown to be an effective method of obtaining concentration dependent gas measurements both at room temperature and at elevated temperatures. Previous work on plasmonic sensors has shown sensitive (ppm level), high temperature (500 °C or greater) sensing responses for analyte gases such as H_2, CO, and NO_2 in the presence of an air based carrier gas.[5−10] The operating principle of these plasmonic sensors is based on the localized surface plasmon resonance (LSPR) property possessed by materials with a high density of free electrons that oscillate in resonance within an electromagnetic field. This oscillation results in absorption or scattering of the incident radiation that can be probed by absorption, reflection or extinction measurements. In addition to an electron density dependence, the LSPR oscillation frequency is also highly dependent on changes to the dielectric environment as dictated by the Drude equation for nanorods given in eq 1:[11]

$$\omega = \sqrt{\frac{N_0 e^2}{(\varepsilon_b + Y_i \varepsilon_m) m_e \varepsilon_0}} \qquad (1)$$

.Equation 1 is the Drude equation modified for nanorod geometry to determine resonant peak frequency (ω): N_0 is the free electron density, e is the elementary charge, ε_b is the interband contribution term, ε_m is

* Address correspondence to mcarpenter@sunycnse.com.

Received for review August 29, 2014 and accepted October 3, 2014.

10.1021/nn504870b

the matrix dielectric constant, Y_i is the shape factor for the ith axis, m_e is the electron mass, and ε_0 is the permittivity of free space.

Nanorods are the focus of this work since they show higher sensitivity than nanoparticles of other geometries such as bipyramids and spheres.[12] Studies on the sensitivity dependence of nanorods for a unit change in the refractive index of the surrounding medium have further shown that the sensitivity is proportional to the aspect ratio, according to the equation:[13]

$$\sigma_{\mathrm{abs}}(\omega) = \frac{V}{3c}\varepsilon_m^{3/2}\sum_{i=1}^{3}(Y_i+1)^2\frac{\omega\varepsilon_2}{(\varepsilon_1+Y_i\varepsilon_m)^2+\varepsilon_2^2} \qquad (2)$$

Equation 2 is the absorption cross section (σ_{abs}) equation for nanorod geometry: V is the particle volume, c is the speed of light in a vacuum, ε_m is the matrix dielectric constant, Y_i is the shape factor for the ith axis which is directly proportional to the aspect ratio, ω is the resonant peak frequency, and ε_1 and ε_2 are the real and imaginary parts of the dielectric function of the metal, respectively.

It can be seen from eq 2 that increasing the nanorod aspect ratio increases sensitivity. Specifically, the condition for resonance in eq 2 is fulfilled when $\varepsilon_1 = -Y_i\varepsilon_m$. By plotting the product of Y_i and ε_m on a graph of ε_1 *vs* wavelength, one can conclude that a nanorod with a higher aspect ratio will exhibit a larger peak shift and more sensitivity for a unit change in the dielectric constant of the matrix compared to a nanorod with a lower aspect ratio. In addition, nanorods show large absorption cross sections at their LSPR resonance wavelengths. Jain *et al.* have shown that gold nanorods exhibit a size-normalized absorption coefficient that is over an order of magnitude larger than other geometries such as nanospheres and nanoshells.[14] By fabricating nanorods with electron beam lithography, the degree of tunability of the rods is enhanced, which allows creation of optimal nanorod samples for use in environments with different temperatures and thus different distributions of thermally radiated photons. Furthermore, analyte gases can react and alter either the free electron density or the dielectric environment surrounding the plasmonically active nanoparticle such that its LSPR frequency shifts upon gas exposures. For this reason, the LSPR peak frequency (wavelength) and the corresponding absorption spectrum are common observables used in plasmonics-based gas sensing experiments.

Au nanoparticles have shown great promise in plasmonics-based sensing due to their high resistance to oxidation and their shape dependent catalytic and plasmonic properties.[15−19] In particular, Au particles with nanorod geometries have been demonstrated in the literature to show highly tunable SPR properties based on their aspect ratio (ratio of rod length to width).[13,20] Rods that have higher aspect ratios have a red-shifted longitudinal LSPR peak. This allows the nanorods to be tuned to different absorption wavelengths, convenient for a diverse set of applications. Furthermore, Au nanorods have been shown to be stable at high temperatures when encapsulated within a yttria-stabilized zirconia (YSZ) overcoat layer. Specifically, Joy *et al.* have shown that Au nanorods with a yttria-stabilized zirconia (YSZ) overcoat layer give repeatable high temperature, 500 °C, sensing results for H_2, CO, and NO_2 in an air carrier gas.[21]

While it is clear that an array of embedded sensors is ideal for obtaining accurate sensing information, drawbacks of existing optical sensor technology include size and cost limitations which hinder the placement of multiple sensors in optimal feedback locations.[22] This limitation is a result of optical sensing approaches typically requiring both a spectrometer to probe and track optical properties and an external incident light source. Integrating multiple spectrometers into a sensing application is not practical due to both size and cost limitations and further miniaturization of this hardware component is challenging. However, with the use of a data analysis method such as principal component analysis (PCA), the number of monitored wavelengths required to identify analyte gases can be reduced, while retaining a significant amount of important information about the data.[23,24] By selecting the optimal wavelengths to monitor, one can foresee reducing the required detector from a full-size spectrometer down to several diode detectors combined with narrowly tuned bandpass filters so that only those selected wavelengths are monitored as a function of time and exposure.

All previous sensing studies, which employ a plasmonic-based sensing approach use an external incident light source to probe the plasmonic properties of the sensing structure. However, when plasmonic-based emission gas sensors are used in combustion environments, there is an ample amount of thermal radiation due to operating temperatures that can range between 500 and 800 °C, and thus, it is possible to harvest this thermal radiation for optical measurements. Such a thermal energy harvesting method would eliminate the need for an external incident light source, simplify the system design, and favor integration of the sensing system into industrial scale applications. Combining this approach with a PCA-enabled wavelength reduction process offers a method toward easing the integration concerns noted above.

Thermal radiation is a property of any blackbody above absolute zero and is a consequence of molecular vibrations with the resulting intensity and energy distribution of emitted thermal radiation being dependent on the temperature of the body. As the temperature of a blackbody is increased, the magnitude of its spectral radiance is increased according to

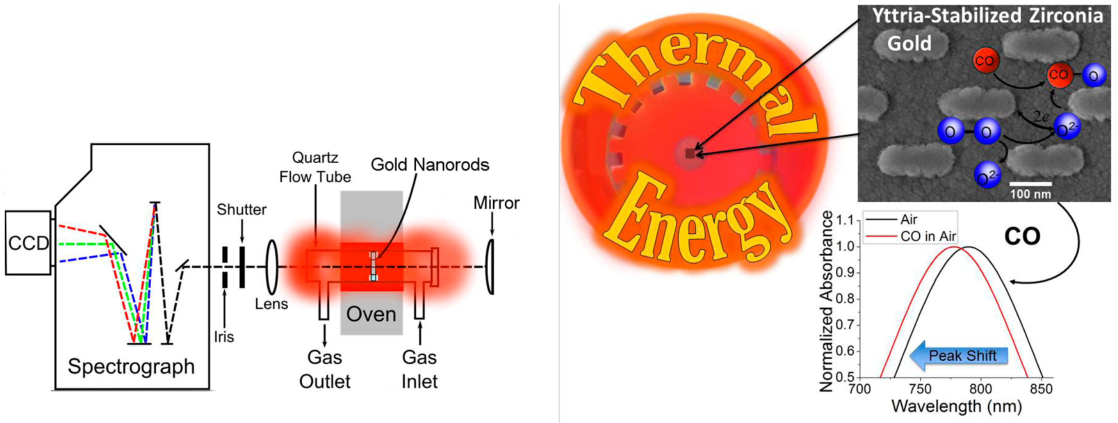

Figure 1. (Left) Schematic of the thermal imaging bench setup. (Right) Diagram showing the placement of the sample in the macor holder inside the furnace. Interfacial surface reactions between CO and oxygen species are also shown.

Planck's law:

$$U(\lambda) = \frac{8\pi h v^3}{c^3\left(\exp\left(\frac{hc}{\lambda kT}\right) - 1\right)} \tag{3}$$

Equation 3 is Planck's law to determine the spectral radiance as a function of wavelength, $U(\lambda)$, in units of energy per volume per unit wavelength, where h is the Planck constant, λ is the wavelength of thermally radiated light, c is the speed of light in a vacuum, k is the Boltzmann constant, and T is the temperature of the heated body.

The distribution of spectral radiance at temperatures in the range of 500–800 °C has a maximal radiance wavelength in the infrared region. However, there is a higher energy "tail" to these distributions that show there is a fraction of the total spectral radiance occurring in the visible and near-infrared light region. This radiation therefore has potential to be exploited for plasmonic gas sensing by an appropriately designed sample that can harvest or absorb this energy.

Work by Greffet *et al.* shows that coherent thermal emission can be achieved on the microscale and an infrared source can be made coherent over distances as large as 0.6 mm.[25] Han and Norris show that a tungsten bulls-eye comprised of smooth concentric circular rings can be engineered such that when heated it emits a single beam of light that shows a narrow degree of angular divergence (~0.021° at its fwhm).[26] The bulls-eye approach can theoretically be tuned to harvest energy in the visible and near-infrared by changing the patterned metal from tungsten to either Au or Ag and also modifying the concentric ring dimensions. While utilizing a patterned, plasmonically active material in a bulls-eye pattern is one method to harvest thermal radiation, this method presents another significant challenge in that the material must be made thermally stable under the harsh environment conditions that are the target of this work.

A further obstacle is that thermal radiation is isotropic and nondirectional as in an incandescent lightbulb.[25] This obstacle can be overcome if the thermal radiation source mimics a weak white light source *via* an apparatus designed to direct the thermal radiation such that an absorbance measurement could be obtained. If this radiation is directed through a plasmonically active chemical sensor, with appropriate referencing to Planck's spectral radiance equation, it is expected that chemical sensing observations can be obtained that are similar to when an external incident light experiment is performed.

RESULTS AND DISCUSSION

As a demonstration of the general and simpler methodology described above, this study has replaced the external incident white light source with a mirror at the entrance of a tube furnace as shown in the schematic of Figure 1 (left). With proper mirror alignment, a fraction of the emitted light from the furnace is reflected back through the sample, housed within a quartz flow cell, thus more closely mimicking a low intensity quasi-directional coherent white light source. At above 600 °C, the thermal radiation emitted by the furnace is strong enough in the visible region of the spectrum that the thermal radiation is harvested by the plasmonically active sensing material, thereby enabling an absorbance measurement experiment to be performed. The thermally harvested LSPR absorption spectrum is then monitored as a function of time and changes in analyte gas concentration (referred to in this article as thermal imaging experiments). Characteristic changes in the LSPR spectrum are then calibrated for selective detection of the analyte gas.

To have Au nanoparticles which have a strong absorption cross section in the high energy "tail" region of the blackbody radiation from the furnace, patterned Au nanorods were used because of their advantages in being easily tuned through modification of its aspect ratio.

The spectral overlap of the LSPR absorption spectrum with both the thermal energy emitted by the tube furnace operating at 600 °C (both scaled and offset for clarity) as well as the calculated spectral irradiance from Planck's distribution are displayed in Figure 2 and are an indication of the feasibility of this proposed methodology. Both thermal imaging and white light imaging spectra were then acquired individually as a function of time and H_2, CO, and NO_2 gas exposure concentrations at an operating temperature of 510 °C in an air carrier gas. A comparison of the thermal imaging and the white light LSPR peak position *vs* time data as a function of analyte gas concentration is shown in Figures 3–5.

The data shown in Figures 3–5 exhibit the expected trends: a blue shift in plasmon peak position for reducing gases and a red shift in peak position for oxidizing gases. The mechanism behind this has been elucidated in the literature and is based on the Drude equation given above which shows a direct dependence of the peak frequency on the free electron density and an indirect dependence on the matrix dielectric constant.[7,8] The proposed reaction mechanisms for both H_2 and CO are interfacial charge transfer reactions, which include adsorption followed by reaction forming H_2O and CO_2 through removing oxygen anions from the lattice followed by electron transfer to the gold nanoparticles. Electron transfer to the Au particles decreases the polarizability and the dielectric function of the metal oxide matrix and induces a blue shift in the LSPR wavelength. This mechanism has been proposed from previous titration experiments using a white light type experiment.[7] The reaction mechanism proposed for NO_2 is dissociative adsorption forming NO and O, and then O radical ionization *via* electron transfer. The electron transfer removes electrons from the Au nanorods to form oxygen anions and, in doing so, increases the polarizability and the dielectric function of the matrix, thus inducing a red shift in the LSPR wavelength.[8] This type of mechanism for NO_2 is not unexpected as it has been previously shown to catalytically react on heated gold–metal oxide surfaces.[27] Since the number of incident photons is higher for the white light imaging as compared to thermal imaging, a higher number of generated hot carriers are expected in the white light measurements due to the increased intensity of the generated plasmonic fields. As studies have shown, hot electrons, as they extend further away from the nanoparticle, can facilitate reactions such as H_2 dissociation on Au.[28] Thus, we expect to see an increased magnitude of reaction when using a white light source and hence an increased peak shift magnitude. Generally, each type of experiment in this study had response and recovery times of 300 s or greater and will need to be improved with further studies prior to industrially relevant applications. The results shown in Figures 3–5 are also repeatable, as shown by the 20+ h of experimental testing through the noted gas cycles.

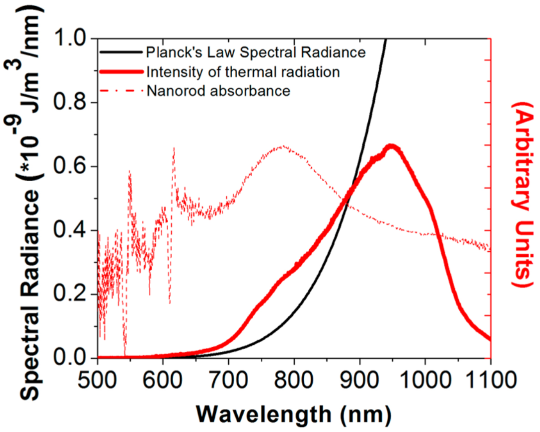

Figure 2. Comparison of the experimentally collected thermal intensity spectrum emitted from the thermal imaging bench (solid red line), the nanorod absorbance spectrum (dashed red line), and the expected theoretical spectrum calculated from Planck's law eq 1 at 700 °C (black line). Note: the furnace emission curve will peak at wavelengths well beyond the 1100 nm detection limit of the CCD spectrograph that was used in this experiment.

Figure 6 shows calibration plots for the Au nanorods, which plot the change in the centroid peak position determined from the polynomial fit to the LSPR spectra as a function of H_2, CO, or NO_2 concentration for both the thermal imaging and white light experiments. The plots show a sensitive response at low concentrations.

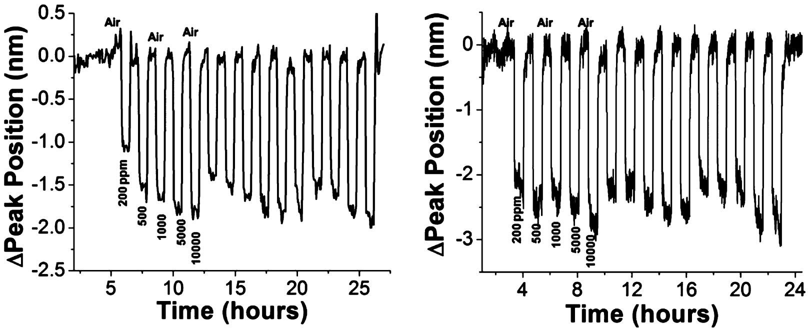

Figure 3. Sensing results for air–H_2 mixture. H_2 concentrations: 200, 500, 1000, 2000, 10 000 ppm. Thermal imaging data (left), white light data (right), gas on and off times for both experiments are 40 min.

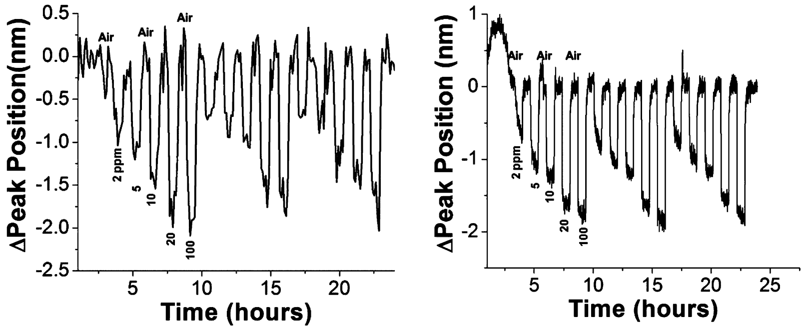

Figure 4. Sensing results for air–CO mixture. CO concentrations: 2, 5, 10, 50, 100 ppm. Thermal imaging data (left), white light data (right), gas on and off times for both experiments are 40 min.

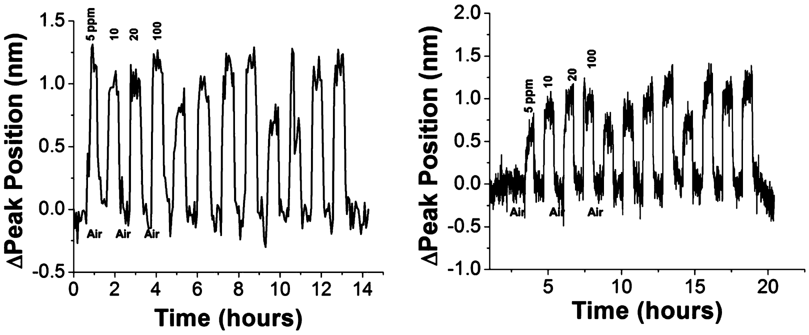

Figure 5. Sensing results for air–NO_2 mixture. NO_2 concentrations: 5, 10, 20, 98 ppm. Thermal imaging data (left), white light data (right), gas on and off times for both experiments are 40 min.

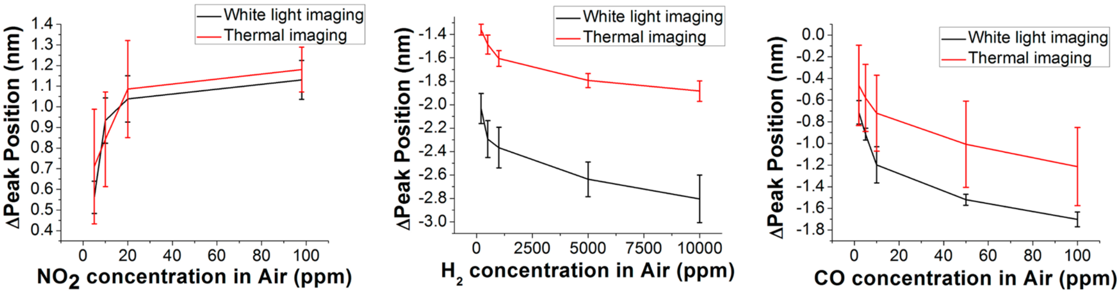

Figure 6. Calibration plots from thermal imaging and white light imaging data for NO_2 (left), H_2 (middle), and CO (right) analyte gases in an air background.

At lower concentrations of an analyte gas, the slope for the white light imaging experiment is steeper for all gases considered. The reason for this could be due to a plasmonically activated hot electron transfer reaction mechanism *via* the increased electron–hole pairs generated,[29,30] which is not as prevalent in the thermal imaging results due to the reduction in incident photons. At larger analyte gas concentrations, the white light and thermal imaging plots have nearly identical slopes. The dissociation of NO_2 and the availability of sites for the resulting oxygen anions depend on the availability of oxygen vacancies in the YSZ layer. As the sample is purged with air before the start of NO_2 exposures, it is likely that the oxygen vacancies are at least partially saturated, and this would be the reason for a reduced rate of NO_2 dissociation and hence the reduced magnitude of peak shift for NO_2 as compared to H_2 and CO. Furthermore, as there is no appreciable difference between the white light and thermal imaging data for the NO_2 experiments, we can speculate at this point that plasmonic enhancement (as discussed above) is not a dominant factor for this reaction. Furthermore, at this point there is not enough information to speculate on the differences observed between the H_2 and CO peak shift magnitudes, but future interfacial mechanism studies may allow for a determination of the detailed mechanism.

The collected thermal imaging data has larger error bars due to two reasons: (a) the number of measurements collected per time period and (b) the lower signal-to-noise (S/N) ratio in these measurements. Fewer measurements are collected in the thermal imaging because of the large exposure times required to obtain a single measurement and the high averaging that is used to improve the S/N ratio. Comparing the thermal imaging calibration curves, the error bars

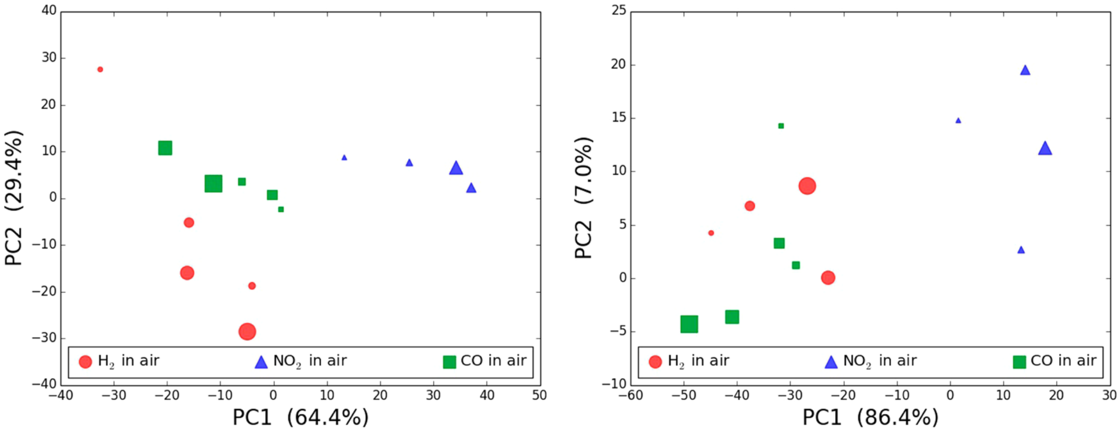

Figure 7. White light full spectrum PCA (left) and thermal imaging full spectrum PCA (right).

for H_2 are smaller than those for both NO_2 and CO. This is a result of the different collection times used as discussed in the Methods section. These collection parameters resulted in a higher number of available points per cycle for H_2 than for both CO and NO_2, which gives a lower error when all the available points are averaged. The percent error for the white light H_2 test, while comparable to that from the white light tests for both CO and NO_2, appears large when compared to a particularly good thermal test that also averages a higher number of values as discussed above. Improvement of the S/N ratio in the thermal imaging measurements can be handled by exchanging the reflection mirror with a focusing mirror, which would increase the number of photons that pass through the sample and are collected by the spectrometer. Furthermore, when nanorods are patterned with dimensions such that they harvest thermal energy further in the near-infrared region (1000−2000 nm), their absorption cross section maxima will overlap with a higher number of emitted photons as illustrated by the Planck distribution equation, which should also lead to an improved data set.

While the current work has demonstrated for the first time that a plasmonics-based chemical sensing experiment does not necessarily require an external incident light source, another feature that can be optimized in the sensor design is miniaturizing and simplifying the detector component. Given cost and space considerations, a spectrometer is not practical for integration into emission gas mapping systems for combustion environment applications. Realistically, in order to integrate an optical sensor, a selective wavelength detection approach needs to be taken. One such avenue would be using narrow band-pass filters combined with diode detectors such that each would monitor a single wavelength. The wavelengths to be monitored would be those that have the greatest impact on the total variation in the data. A method of data analysis that has shown great promise in providing the necessary information for analyte gas discrimination using the above principle is principal component analysis (PCA).[23,24,31,32]

PCA performs dimensional reduction by generating PC vectors that are linear combinations of the original input variables. The PC vectors lie in directions of maximum variance in the data and are orthogonal to each other. Projection of a combination of principal components onto a subspace is known as a scores plot. The scores plot of the first several principal components usually describes most of the variance present in the data. PCA has been completed for both the white light and the thermal imaging data using the difference spectra obtained from subtracting the LSPR gas-on spectrum from the LSPR gas off spectrum (both spectra were first fitted using the same polynomial routine noted above to reduce random variances in the data set and then smoothed using the Savitzky-Golay algorithm) followed by autoscaling preprocessing for each of the concentrations used in the H_2, CO, and NO_2 experiments. Subtraction of the gas spectra was done after completion of the experiment as a separate step in the data analysis. The difference spectra were limited to the wavelength region between 600 and 1000 nm in order to cut out the regimes where noise was dominant, which would negatively influence the PCA analysis. The resulting PC scores plot is displayed in Figure 7 for both the white light and thermal imaging experiments.

The white light data shown in Figure 7 shows a unique gas response for the three analyte gases. This unique response means that a single Au nanorod−YSZ nanocomposite reacts differently to these gases and could be used to distinguish between H_2, NO_2, and CO in a system with an unknown combination of these gases. The thermal imaging data has issues distinguishing between the two reducing gases but with an improved S/N ratio, a more absolute picture will be possible. A determination of the down selected wavelengths to use for a reduced data set PCA analysis was completed through inspection of the overlaid LSPR spectra for gas on and off conditions and the resulting

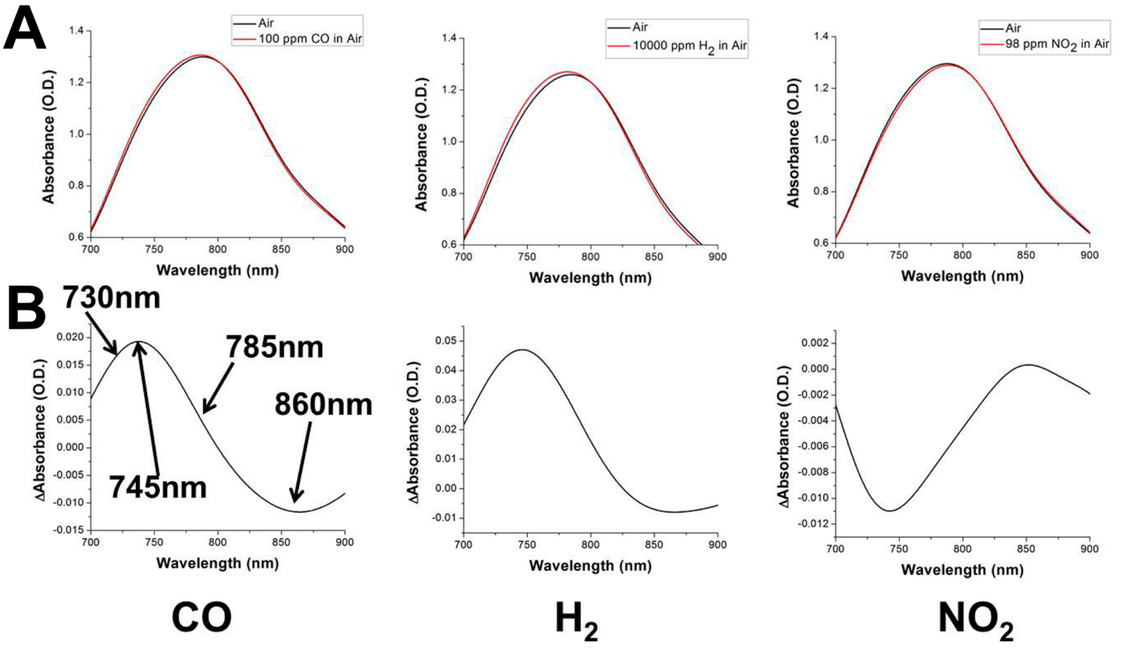

Figure 8. (A) Overlay of the gas on/gas on spectra (top row) and (B) corresponding difference spectra (bottom row) for the highest concentrations of each of the three analyte gases for CO (left), H_2 (middle), and NO_2 (right). Arrows on the CO difference spectrum point to the location of the four selected wavelengths.

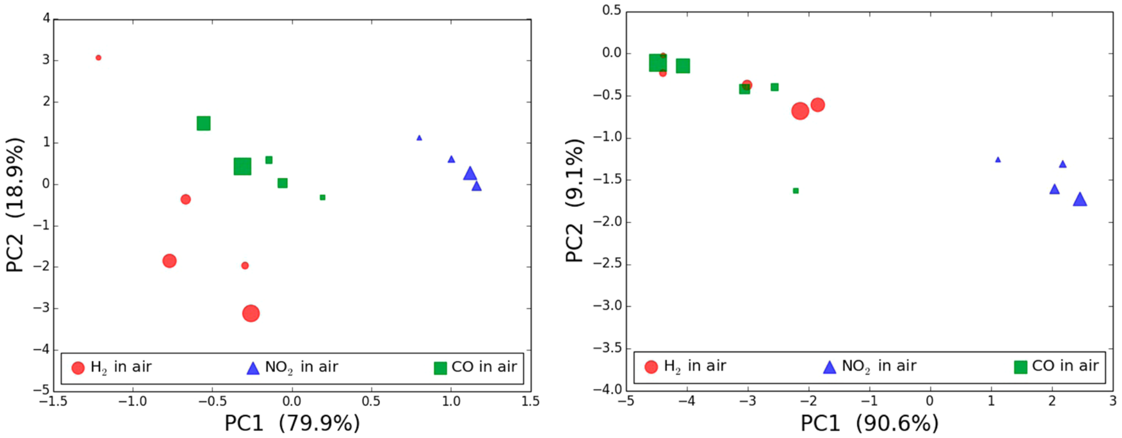

Figure 9. White light PCA done with wavelength reduction (left). Thermal imaging PCA done with wavelength reduction (right). Four wavelengths (730, 745, 785, and 860 nm) were chosen for the plot.

difference spectra used to produce the PC scores plots in Figure 7. Examples of the overlaid LSPR and their corresponding difference spectra are displayed in Figure 8, panels A and B, respectively, for the highest concentrations used in the white light experiment. Arrows in this figure show wavelengths at 730, 745, and 860 nm that displayed significant differences, with 785 nm being the wavelength closest to the LSPR peak position during the air gas cycle. In doing the wavelength reduction, the PCA input wavelength variable set is reduced from 665 to 4. Rerunning the PCA analysis with this reduced wavelength data set generates the PC scores plot for both the white light and thermal imaging experiments, which is shown in Figure 9.

Inspection of Figures 8A and 9 shows that with this approach an even greater separation has been achieved for the white light imaging experiment between the reducing gas clusters than with the full spectrum analysis. A conclusion from this analysis is that a full absorption spectrum obtained using an imaging CCD spectrometer is not necessary. In fact, the experiment could be as simple as monitoring the intensity changes at 730, 745, 785, and 860 nm as a function of time and emission gas exposure, which could be done with narrow bandpass filters and diode detectors that are referenced to I_o values. Therefore, it is clear that a reduced data set can be used to demonstrate the promise for the selective detection of the target gases. A caveat that is important to note is that achieving both selectivity and sensitivity for mixtures of the analyte gases under these operating conditions requires significant further effort, and likely

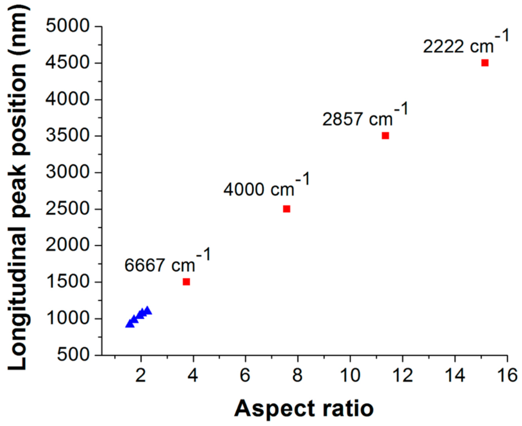

Figure 10. Longitudinal plasmon peak wavelength *vs* nanorod aspect ratio for previously deposited samples as well as predicted plasmon peak positions obtained through linear extrapolation of the experimental data points.

will require analysis of both calibration plots as well as PCA analysis, both of which are currently underway in this laboratory. While the wavelength reduction and PCA analysis approach has not been effectively extended to the thermal imaging data, due to the lower S/N ratio in these measurements, it is expected with an improved S/N ratio that this same approach can be easily and reliably extended to the thermal imaging measurements. In the following section, the barriers that still need to be overcome to allow reduced wavelength analysis for the thermal measurements will be discussed.

At temperatures of 500 °C and above, a large amount of the total thermal irradiance emanates from the near and mid infrared regions. In this article, energy harvesting has been demonstrated in the short wavelength near-infrared region where there is a minority of thermal photon counts. A major advantage with using Au in a nanorod geometry is the proven dependence of the longitudinal peak position on the aspect ratio. When the length of the patterned nanorods, and therefore the aspect ratio, is increased, the longitudinal peak can be shifted further into the near-infrared region if not into the mid-infrared region, which would allow an improved S/N ratio. This characteristic is displayed in Figure 10, which plots the Au longitudinal plasmon peak position as a function of the nanorod aspect ratio. An improved S/N ratio along with the assistance of improved accuracy due to curve fitting will result in an improved calibration curve. The first 5 data points in blue are from nanorod samples previously deposited using the same methods used in the current work. All nanorods had the same width, and ranged in length from 70 to 100 nm, giving aspect ratios between 1.6 and 2.25. Aspect ratios ranging from 3.75 to 15.2 are realized by increasing the rod length to 165 and 667 nm, respectively, and performing a linear extrapolation of the experimental data points. On Figure 10, the red points pertain to the extrapolation of experimentally obtained longitudinal plasmon peaks between 1500 (6667 cm^{-1}) and 4500 nm (2222 cm^{-1}), the latter of which is in an easily accessible region for FTIR spectrometers. Also, as noted before, it is predicted from theory that rods with a higher aspect ratio will exhibit a higher peak shift for a given change in the dielectric constant of the surrounding medium and, hence, a higher sensitivity for a given concentration of an analyte gas.[13] Therefore, one would expect significantly improved results with full spectrum and reduced wavelength PCA. Extending the aspect ratio so that absorbance can occur in the NIR and mid-IR regions would benefit experiments at the current operating temperature of 500 °C as well as lower operating temperatures as the nanorods would be absorbing blackbody radiation closer to the peak in Planck's distribution. However, there are a couple of issues to consider: (1) if low temperatures are to be the target application (100 °C), then thermal stability of the nanorods is less of an issue as stabilization could be done at temperatures as low as 200 or 300 °C;[21] and (2) a change in metal oxide may be needed. YSZ is an excellent oxygen ion conductor at temperatures above 350 °C. However, at the lower temperatures YSZ may not be well suited for these targeted applications and a change in metal oxide matrix material to TiO_2 or CeO_2 or other metal oxide may be needed.

The periodicity that is present in the nanorods has a large effect on the resulting optical properties and can easily be tuned and modified with e-beam lithography. Lin *et al.* have generated an optimal aperiodic array of nanorods that exhibit less reflection loss than both random aperiodic and periodic arrays for use in photovoltaics.[33] Fabricating aperiodic nanorods could also be beneficial for fiber optic applications since the signal needs to be preserved after contacting the plasmonic sensing element in the cable. Future work will address this avenue of research to further optimize the sensing properties of these structures.

Additional optical properties of the Au nanorods that can be explored include plasmonically induced processes like hot electron generation and transfer. Conklin *et al.* have shown that hot electron generation and transfer can be greatly enhanced from plasmons in a Au nanoparticle.[29] Plasmonically induced hot electron transfer has been shown by Mukherjee *et al.* to catalyze the dissociation of H_2.[30] The particle size and hot electron lifetime control the rate of hot electron production and also their energy distribution. Specifically, larger particles produce more hot carriers but with lower energies. As the energy of the hot electrons has been discovered to peak very close to the plasmonic frequency, one can exploit the intense plasmonic excitation for longer nanorods that is expected with this thermal harvesting approach, so that there is an increased rate of hot carrier formation through electron−hole pair generation and possibly increased activity compared to smaller nanorods whose plasmonic excitations peak at lower wavelengths. These photocatalytic processes have been previously demonstrated using an external incident light source. However, it is expected that with proper design of the plasmonically active nanocomposite, the incident light source can be removed and the hot electron generation and transfer processes will still be active in the thermal energy harvesting mechanism. Removal of the need for an external incident light source would again make the integration of photocatalytic processes into industrial standard processes more viable due to the minimization of external hardware requirements.

CONCLUSIONS

In this work, we have shown for the first time that thermal radiation can be effectively harvested in the visible region of the electromagnetic spectrum by plasmonically active Au nanorods, and this method facilitates the collection of absorption spectra without the need for an external incident light source. Gas sensing results using this method of thermal energy harvesting have been performed and compared to white light gas sensing experiments which employ an external light source, and both show strong concentration dependence for the different analyte gases. At lower concentrations, the white light results show higher sensitivity, which is indicative of a plasmonically activated process. Wavelength reduction has been performed using PCA methods, which significantly reduces the number of wavelengths that are required for acquiring effective sensing data. A combination of both thermal harvesting and wavelength reduction has resulted in a new sensing paradigm, which will lead to a highly simplified sensor design that is low cost, reliable, and easier to integrate into emission gas application environments. Extension of these methods into the near- and mid-infrared regions is expected to improve performance as well as having significant impacts on research initiatives with energy and catalytic applications.

METHODS

Nanorod Sample Preparation. The Au nanorods were fabricated with a multistep process involving physical vapor deposition (PVD) and electron beam lithography.[21] Specifically, a 99.9% pure YSZ target was used to deposit a 65 nm thick layer by PVD onto a quartz substrate followed by an annealing procedure. PMMA photoresist was spin-coated on top of the annealed base layer. A chromium layer was then used to serve as a charge-dissipating layer during the patterning step. Next, the sample was patterned with electron beam lithography, followed by Ti and Au depositions using electron beam evaporation. The PMMA resist was then lifted off using acetone. A final 25 nm thick YSZ layer was deposited on top of the Au nanorods to serve as a thermal stabilization layer for the Au nanorods at high temperatures.

Gas Exposure Experiment Details. Gas exposure experiments that used either harvested thermal radiation (referred to as thermal imaging experiments) or an external incident white light source (referred to as white light imaging experiments) were completed. The thermal imaging and white light imaging exposure experiments both used the same Au nanorod–YSZ nanocomposite sample in order to demonstrate H_2, CO, and NO_2 analyte detection in an air background carrier gas. Blank measurements with YSZ alone were not completed as YSZ has a bandgap of nearly 5 eV (250 nm, ~300 nm if in the oxidized state) and thus does not absorb light at the wavelengths of interest used for this study.[34] Optical measurements were obtained with flatfield and background corrections which account for electronic noise and the differences in sensitivity of the CCD array detector. A blank substrate was referenced in real time throughout the experiment to correct for thermal power fluctuations and or white light fluctuations, thereby minimizing baseline drift. A full absorbance spectrum was collected for each spectral acquisition. These absorbance spectra were then fitted using a polynomial fitting approach developed by Dahlin *et al.*,[35] from which the peak position was extracted.

The thermal imaging results were obtained with a furnace temperature of 600 °C, with the measured temperature of the sample being 510 °C. Sensing measurements were conducted using the setup schematically shown in Figure 1 (left). A fraction of the thermally emitted photons reflect off of the mirror and are directed back through the nanorod sample. The photons are then dispersed and detected using a CCD imaging spectrograph to generate an absorbance spectrum, which were obtained through averaging 10 spectra (each with 22 s acquisition time) every 4 min for H_2 and through averaging 10 spectra (each with 22 s acquisition time) every 7 min for CO and NO_2.

White light imaging results were obtained using the same setup as with the thermal imaging results, except that the mirror was removed and a quartz tungsten halogen light source was used. Spectra were collected *via* averaging 10 spectra (each with 0.5 s acquisition time) every 30 s for the duration of the experiment for H_2, CO, and NO_2.

Conflict of Interest: The authors declare no competing financial interest.

Acknowledgment. This work was supported by the United States Department of Energy National Energy Technology Laboratory under contract number DE-FE0007190. Any opinions, findings, and conclusions or recommendations expressed in this publication are those of the authors and do not necessarily reflect the views of the United States Department of Energy National Energy Technology Laboratory.

REFERENCES AND NOTES

1. Carpenter, M. A., Mathur, S., Kolmakov, A., Eds.; *Metal Oxide Nanomaterials for Chemical Sensors*; Springer: New York, NY, 2013.
2. Korotchenkov, G. S.; Dmitriev, S. V.; Brynzari, V. I. Processes Development for Low Cost and Low Power Consuming SnO_2 Thin Film Gas Sensors (TFGS). *Sens. Actuators, B* **1999**, *54*, 202–209.
3. Korotcenkov, G. Gas Response Control Through Structural and Chemical Modification of Metal Oxide Films: State of the Art and Approaches. *Sens. Actuators, B* **2005**, *107*, 209–232.
4. Korotcenkov, G.; Cho, B. K. Instability of Metal Oxide-Based Conductometric Gas Sensors and Approaches to Stability Improvement (Short Survey). *Sens. Actuators, B* **2011**, *156*, 527–538.
5. Ohodnicki, P.; Wang, C.; Natesakhawat, S.; Baltrus, J.; Brown, T. *In Situ* and *Ex Situ* Characterization of TiO_2 and Au Nanoparticle Incorporated TiO_2 Thin Films for Optical Gas Sensing at Extreme Temperatures. *J. Appl. Phys.* **2012**, 111.
6. Sirinakis, G.; Siddique, R.; Manning, I.; Rogers, P.; Carpenter, M. Development and Characterization of Au-YSZ Surface

Plasmon Resonance Based Sensing Materials: High Temperature Detection of CO. *J. Phys. Chem. B* **2006**, *110*, 13508–13511.

7. Rogers, P. H.; Sirinakis, G.; Carpenter, M. A. Direct Observations of Electrochemical Reactions Within Au-YSZ Thin Films *via* Absorption Shifts in the an Nanoparticle Surface Plasmon Resonance. *J. Phys. Chem. C* **2008**, *112*, 6749–6757.
8. Rogers, P.; Sirinakis, G.; Carpenter, M. Plasmonic-Based Detection of NO_2 in a Harsh Environment. *J. Phys. Chem. C* **2008**, *112*, 8784–8790.
9. Larsson, E.; Syrenova, S.; Langhammer, C. Nanoplasmonic Sensing for Nanomaterials Science. *Nanophotonics* **2012**, *1*, 249–266.
10. Ohodnicki, P. R.; Wang, C. J.; Andio, M. Plasmonic Transparent Conducting Metal Oxide Nanoparticles and Nanoparticle Films for Optical Sensing Applications. *Thin Solid Films* **2013**, *539*, 327–336.
11. Kreibig, U.; Vollmer, M. *Optical Properties of Metal Clusters*; Springer: Berlin, 1995.
12. Chen, H. J.; Shao, L.; Woo, K. C.; Ming, T.; Lin, H. Q.; Wang, J. F. Shape-Dependent Refractive Index Sensitivities of Gold Nanocrystals with the Same Plasmon Resonance Wavelength. *J. Phys. Chem. C* **2009**, *113*, 17691–17697.
13. Lee, K. S.; El-Sayed, M. A. Gold and Silver Nanoparticles in Sensing and Imaging: Sensitivity of Plasmon Response to Size, Shape, and Metal Composition. *J. Phys. Chem. B* **2006**, *110*, 19220–19225.
14. Jain, P.; Lee, K.; El-Sayed, I.; El-Sayed, M. Calculated Absorption and Scattering Properties of Gold Nanoparticles of Different Size, Shape, and Composition: Applications in Biological Imaging and Biomedicine. *J. Phys. Chem. B* **2006**, *110*, 7238–7248.
15. Haruta, M. Size- and Support-dependency in the Catalysis of Gold. *Catal. Today* **1997**, *36*, 153–166.
16. Sardar, R.; Funston, A.; Mulvaney, P.; Murray, R. Gold Nanoparticles: Past, Present, and Future. *Langmuir* **2009**, *25*, 13840–13851.
17. Manera, M.; Spadavecchia, J.; Buso, D.; Fernandez, C.; Mattei, G.; Martucci, A.; Mulvaney, P.; Perez-Juste, J.; Rella, R.; Vasanelli, L.; *et al.* Optical Gas Sensing of TiO_2 and TiO_2/Au Nanocomposite Thin Films. *Sens. Actuators, B* **2008**, *132*, 107–115.
18. Julian Fernandez, C. d.; Manera, M. G.; Spadavecchia, J.; Buso, D.; Pellegrini, G.; Mattei, G.; Martucci, A.; Rella, R.; Vasanelli, L.; Guglielmi, M.; *et al.* Gold/Titania Nanocomposites Thin Films for Optical Gas Sensing Devices. *Proc. SPIE* **2005**, *5836*, No. 703.
19. Della Gaspera, E.; Bersani, M.; Mattei, G.; Nguyen, T.; Mulvaney, P.; Martucci, A. Cooperative Effect of Au and Pt inside TiO_2 Matrix for Optical Hydrogen Detection at Room Temperature Using Surface Plasmon Spectroscopy. *Nanoscale* **2012**, *4*, 5972–5979.
20. Perez-Juste, J.; Pastoriza-Santos, I.; Liz-Marzan, L.; Mulvaney, P. Gold Nanorods: Synthesis, Characterization and Applications. *Coord. Chem. Rev.* **2005**, *249*, 1870–1901.
21. Joy, N.; Janiszewski, B.; Novak, S.; Johnson, T.; Oh, S.; Raghunathan, A.; Hartley, J.; Carpenter, M. Thermal Stability of Gold Nanorods for High-Temperature Plasmonic Sensing. *J. Phys. Chem. C* **2013**, *117*, 11718–11724.
22. Ohodnicki, P.; Buric, M.; Brown, T.; Matranga, C.; Wang, C.; Baltrus, J.; Andio, M. Plasmonic Nanocomposite Thin Film Enabled Fiber Optic Sensors for Simultaneous Gas and Temperature Sensing at Extreme Temperatures. *Nanoscale* **2013**, *5*, 9030–9039.
23. Joy, N. A.; Nandasiri, M. I.; Rogers, P. H.; Jiang, W. L.; Varga, T.; Kuchibhatla, S.; Thevuthasan, S.; Carpenter, M. A. Selective Plasmonic Gas Sensing: H_2, NO_2, and CO Spectral Discrimination by a Single Au-CeO_2 Nanocomposite Film. *Anal. Chem.* **2012**, *84*, 5025–5034.
24. Rumyantsev, S.; Liu, G. X.; Potyrailo, R. A.; Balandin, A. A.; Shur, M. S. Selective Sensing of Individual Gases Using Graphene Devices. *IEEE Sens. J.* **2013**, *13*, 2818–2822.
25. Greffet, J.; Carminati, R.; Joulain, K.; Mulet, J.; Mainguy, S.; Chen, Y. Coherent Emission of Light by Thermal Sources. *Nature* **2002**, *416*, 61–64.
26. Han, S.; Norris, D. Beaming Thermal Emission from Hot Metallic Bull's Eyes. *Opt. Express* **2010**, *18*, 4829–4837.
27. Bollinger, M. J.; Sievers, R. E.; Fahey, D. W.; Fehsenfeld, F. C. Conversion of Nitrogen Dioxide, Nitric Acid, and *n*-Propyl Nitrate to Nitric Oxide by Gold-Catalyzed Reduction with Carbon Monoxide. *Anal. Chem.* **1983**, *55*, 1980.
28. Mukherjee, S.; Zhou, L. A.; Goodman, A. M.; Large, N.; Ayala-Orozco, C.; Zhang, Y.; Nordlander, P.; Halas, N. J. Hot-Electron-Induced Dissociation of H_2 on Gold Nanoparticles Supported on SiO_2. *J. Am. Chem. Soc.* **2014**, *136*, 64–67.
29. Conklin, D.; Nanayakkara, S.; Park, T. H.; Lagadec, M. F.; Stecher, J. T.; Chen, X.; Therien, M. J.; Bonnell, D. A. Exploiting Plasmon-Induced Hot Electrons in Molecular Electronic Devices. *ACS Nano* **2013**, *7*, 4479–4486.
30. Mukherjee, S.; Libisch, F.; Large, N.; Neumann, O.; Brown, L. V.; Cheng, J.; Lassiter, J. B.; Carter, E. A.; Nordlander, P.; Halas, N. J. Hot Electrons Do the Impossible: Plasmon-Induced Dissociation of H_2 on Au. *Nano Lett.* **2013**, *13*, 240–247.
31. Joy, N. A.; Rogers, P. H.; Nandasiri, M. I.; Thevuthasan, S.; Carpenter, M. A. Plasmonic-Based Sensing Using an Array of Au-Metal Oxide Thin Films. *Anal. Chem.* **2012**, *84*, 10437–10444.
32. Dharmalingam, G.; Joy, N. A.; Grisafe, B.; Carpenter, M. A. Plasmonics-Based Detection of H_2 and CO: Discrimination between Reducing Gases facilitated by Material Control. *Beilstein J. Nanotechnol.* **2012**, *3*, 712–721.
33. Lin, C. X.; Huang, N. F.; Povinelli, M. L. Effect of Aperiodicity on the Broadband Reflection of Silicon Nanorod Structures for Photovoltaics. *Opt. Express* **2012**, *20*, A125–A132.
34. PaiVerneker, V. R.; Petelin, A. N.; Crowne, F. J.; Nagle, D. C. Color-Center-Induced Band-Gap Shift in Yttria-Stabilized Zirconia. *Phys. Rev. B* **1989**, *40*, 8555.
35. Dahlin, A. B.; Tegenfeldt, J. O.; Hook, F. Improving the Instrumental Resolution of Sensors Based on Localized Surface Plasmon Resonance. *Anal. Chem.* **2006**, *78*, 4416–4423.